A Configuration of Storage System for DC Microgrids

Ming-Hao Wang, *Student Member, IEEE,* Siew-Chong Tan, *Senior Member*, Chi-Kwan Lee, *Senior Member, IEEE,* and S. Y. (Ron) Hui, *Fellow, IEEE,*

***Abstract*—Battery energy storage systems (BESS) are often adopted to buffer the difference between the intermittent solar power and the load demand in power grids. The costs of such PV-battery systems increase as the required energy storage increases. In this paper, a new configuration comprising the photovoltaic (PV) panels, a series DC electric spring (series ES) and a non-critical load is proposed to reduce the battery storage capacity of DC microgrids that have substantial PV installations. This arrangement forms a PV-embedded series DC electric spring (PVES). An optimization method considering the minimization of electricity bills of the DC microgrids is included to size the storage capacity and to determine the rating of the PV that are connected to the series ES. Experiments on a 48 V isolated DC grid and simulations on a 400 kVA grid-connected DC microgrid have been conducted to verify the storage reduction feature of the PVES. Both sets of results show that the PVES can tackle the intermittency of the solar power with a smaller storage capacity than that typically required in DC grids with PV installations.**

***Index Terms*—Smart load, power electronics, PV system, electric springs, storage reduction, DC grids.**

NOMENCLATURE

$1-x$	Shifting coefficient, which denotes the proportion of PVs being shifted from the mains to the DC-link of the ES.
α	Proportion of total NCL energy consumption.
β	Penetration depth of the solar power.
η_G, η_B	Power conversion efficiency of the main DC source and battery, respectively.
κ	Absolute ratio of the P_{ES} over the power change of smart load (ΔP_{SL}).
ρ_B, ρ_G	Ramping rate of P_B and P_G, respectively.
ε	The tolerable deviation of the smart load energy after a cycle of N.
ξ	The tolerable deviation of the battery energy after a cycle of N.
B	Real-time electricity price.
C_{BESS_GC}	Accumulated electric bill of the BESS-integrated grid-connected DC microgrids.
C_{PVES_GC}	Accumulated electric bill of the PVES-integrated grid-connected DC microgrids.
$G_{\Delta d}$	Duty ratio to ES output voltage transfer function.
i_B	Battery current flowing from the cathode to the anode.
i_{ESD}	Averaged current (over a switching cycle) flowing from the DC-link of the ES converter to the grid side.
i_s	Current of the shifted PV module.
P_C, P_{NC}	Power of critical and non-critical loads.
P_{ES}	Power of the electric spring.
P_{G_max}, P_{B_max}	Power limits of the main DC source and battery, respectively.
P_G	Generated power of the main DC source.
P_{OS}	Power difference between the total generation and load.
P_{SL}	Power of the smart load.
P_{solar}	Generated power of the PV panels.
PCC	Point of common coupling.
R_L	Resistance of the distribution cable.
R_{NC}	Resistance of the non-critical load.
S^{BESS}	Required storage capacity of the BESS integrated DC microgrid.
S^{PVES}	Required storage capacity of the PVES integrated DC microgrid.
V_B	Voltage of the battery.
V_{ES}	Output voltage of the electric spring.
V_{PCC}	Voltage at PCC.
V_{ref}	Reference voltage at PCC.

In this paper, unless otherwise specified, $|\cdot|^n$ denotes the discretized value of variable $|\cdot|$ at n's time step.

The authors are with Department of Electrical and Electronic Engineering, The University of Hong Kong, Hong Kong. S. Y. R. Hui is also with Department of Electrical and Electronic Engineering, Imperial College London, U.K. This work was supported by the Hong Kong Research Grant Council under the Theme-based Project T23-701/14-N. This paper was presented in part at the IEEE Applied Power Electronics Conference and Exposition 2016, Long Beach, CA, USA.

I. INTRODUCTION

The DC distribution grid is a promising grid infrastructure interfacing a range of electronic loads including plug-in hybrid electric vehicles (PHEVs) [1] and distributed renewable generations. For a DC grid installed with PV generations, battery energy storage system (BESS) is usually applied to buffer the intermittent solar generations. This PV-battery combination can bring the benefits of peak load shaving, reduction of electric bills [2], and improvement in energy efficiency of the grid [3]. Nevertheless, the use of BESS will increase the infrastructure cost and introduce potential environment problems [4]. Thus, it is desirable to minimize the installation capacity of the battery while achieving a satisfactory grid regulation.

Existing technologies for the reduction of battery capacity can be generally categorized into (i) optimum sizing and control of BESS, (ii) generation side management (GSM) and (iii) demand side management (DSM). In IEEE Standard 1013-2007 [5], a battery sizing procedure for standalone PV

systems is provided. In [6], an optimization method of storage sizing for grid-connected PV systems with considerations of the electric bills reduction and time-of-use (TOU) tariff is reported. In [7], a cascaded coordinative control method is introduced for the reduction of storage capacity. A shared energy storage scheme is proposed in [8] to maximize the usage of the storage capacity. However, these technologies do not fundamentally reduce the mismatch between solar generation and users' load profile. Thus, the capacity of the BESS is inevitably increasing with the scales of PVs [9].

With the GSM approach, the energy imbalance between the generations and loads can be reduced by the active control of both the renewable energy sources (RES) and the primary generators [10]. Consequently, the required battery capacity for energy buffering will be smaller. In [11], both utility-interfaced converter and the RES are controlled to follow an hours-ahead power reference, which thereby reduces the size of the battery storage. In [12], [13], a peak solar power curtailment control is adopted to prevent over-generation of power so as to achieve a reduced storage size. However, an immediate drawback of these GSM approaches is the wastage of PV generation capacities [12].

The DSM approaches are based on the principle of varying the load to follow the generation profile to achieve a smaller storage size. Typical methods of remote on/off control of loads and adopting the TOU tariff cannot realize real-time power balance and smooth load transition. In [14], a concept of controllable loads is introduced. The heat pump air conditioner can be operated as an energy buffer to reduce the storage capacity. In [15], it is reported that loads can be operated as bus voltage regulating units to compensate the power fluctuations in DC grids. The utilization of the controllable load capacity can reduce the mismatch of generation and demand, while allowing the RES to be operated at maximum power point. Therefore, the DSM approaches can be considered as cost-effective means for the reduction of energy storage capacity.

In [16], series DC electric springs (series ES) are proposed to regulate bus voltages for DC grid systems. It is a power-electronic-based distributed DSM technology. Each ES is connected in series with a non-critical load (NCL) to form a smart load. It can (i) regulate the bus voltage variation, (ii) compensate the harmonics [17] and (iii) provide fault-ride-through services in the DC grids [18]. The series ES distinguishes itself from other DSM technologies with its independency of communication networks, the real-time manipulation of NCL and the on-site voltage support. Though the series ES can balance the generation and load profiles through the manipulation of NCL, it has to output a significant amount of energy when suppressing the system voltage. Hence, a sufficiently large energy storage is needed if the power imbalance prolongs.

In this paper, a new configuration of PV-embedded series DC electric spring (PVES) is proposed to reduce the storage capacity of PV-integrated DC grids. Some of the PV panels are shifted from the grid to the DC-link of the series ES to form a PV-ES-NCL unit. The shifted part of the PV panels can help the series ES to output energy when the ES is operated to suppress the system's voltage. Since the output power no longer comes solely from the storage unit, the size of the battery can be significantly reduced. This paper is an extension of [19]. The detailed optimization formulae considering the minimization of electricity bills of the DC microgrids are provided. The impacts of PVES on the required storage capacity in both isolated and grid-connected DC microgrids are analyzed. Experimental and simulation results showing that the new combination of PV-ES-NCL unit requires less storage capacity to buffer the intermittent solar generation than the traditional BESS (PV-battery unit), will be provided.

II. PV-INTEGRATED DC MICROGRIDS

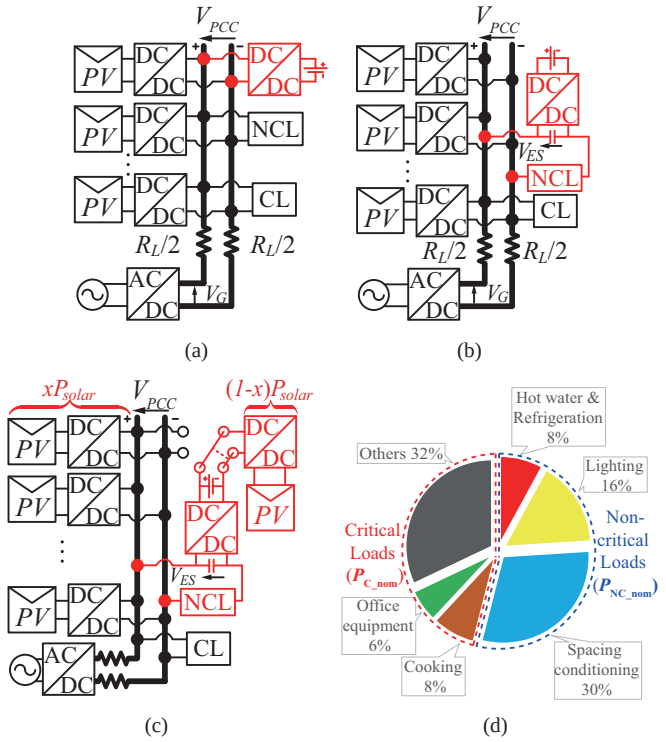


Fig. 1. Equivalent circuits of PV-integrated DC microgrids under various storage configurations: (a) BESS, (b) series ES, and (c) PVES. $1-x$ is the PV shifting coefficient, which quantifies the amount of the original grid-connected PVs that is shifted to the series ES, $0 \le x \le 1$. (d) Proportions of commercial energy end-use in Hong Kong [20].

A. Main DC Source

The schematic diagrams of the typical PV-integrated DC microgrids installed with BESS, series ES and PVES, are respectively shown in Fig. 1(a), 1(b) and 1(c). The main DC source delivers a base power P_G to the grid through the distribution cables with a resistance of R_L. In a grid-connected microgrid, the DC source, which is typically a bi-directional AC–DC converter, can exchange power with the AC utility grid to engage the users in energy market trading.

In an isolated microgrid, the DC source, which can be a DC generator, will provide a well-regulated terminal voltage V_G. For both cases, the bus voltage V_{PCC} will be regulated to V_{ref} by the voltage regulation mechanisms. In this paper, they are namely the BESS, the series ES and the PVES.

B. PV Generation System and Solar Power Profile

As shown in Fig. 1, the modular structure is often adopted in PV generation for its high efficiency, scalability and plug-and-play feature [21], [22]. The DC–DC converters operate the PVs at the maximum power point (MPP) via a maximum power point tracking (MPPT) control. Thus, the time profiles of solar power P_{solar} will follow the pattern of the irradiance profiles as shown in Fig. 2(a). To evaluate the scales of the integrated PVs in the microgrids, we define the penetration depth of the solar power as

$$\beta = \frac{Total\ Generated\ Solar\ Energy}{Total\ Load\ Consumption} = \frac{\int_0^{T_D} P_{solar} dt}{\int_0^{T_D} (P_{NC} + P_C) dt} \quad (1)$$

where T_D is the evaluation period. P_{NC} and P_C are the power of the NCLs and CLs.

C. Load Classification and Load Profile

According to Fig. 1(d), the loads can be classified into (i) critical load (CL), which demands a tightly regulated supply voltage and (ii) non-critical load (NCL), which has a certain tolerance to a variable supply voltage. In this work, the NCL is considered to be purely resistive and passive (e.g., water heater). Fig. 1(d) illustrates the proportions of commercial energy end-use in Hong Kong. The NCL proportion α is defined as

$$\alpha = \frac{Total\ NCL\ Energy}{Total\ Load\ Consumption} = \frac{\int_0^{T_D} P_{NC} dt}{\int_0^{T_D} (P_{NC} + P_C) dt} \quad (2)$$

For the examples shown in Fig. 1(d), α is around 50%.

Fig. 2(b) illustrates the scaled-down hourly-averaged daily load profiles of a microgrid in Denmark [24]. Comparing Fig. 2(a) and 2(b), the power generation does not match the load consumption. Thus, a sufficiently large storage system is needed to buffer the supply-demand imbalance.

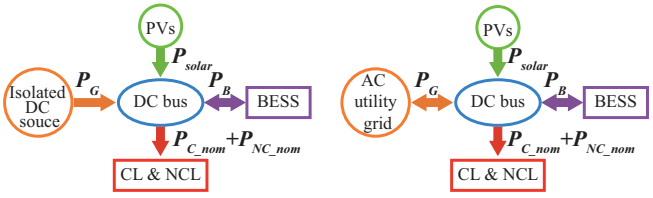
III. Energy Management Analysis in DC Microgrids

By neglecting the power loss on the distribution cable, the difference between the total generation and load can be calculated as

$$P_{OS} = P_G + P_{solar} - P_{C_nom} - P_{NC_nom}\ , \quad (3)$$

where P_{C_nom} and P_{NC_nom} are the nominal time profiles of the CL and NCL, respectively.

A. DC Microgrids with the BESS



(a) Isolated DC microgrids (b) Grid-connected DC microgrids

Fig. 3. Illustrations of power flow paths of BESS integrated DC microgrids.

The power flow paths of a BESS integrated DC microgrid for both cases of isolated and grid-connected configurations are shown in Fig. 3. For an isolated DC microgrid (Fig. 3(a)), P_G can be calculated by

$$P_G = \frac{V_G - V_{ref}}{R_L} \times V_G \quad (4)$$

The BESS will store or deliver energy to balance the generations and the loads.

In grid-connected DC microgrids (Fig. 3(b)), based on the real-time electricity prices, the users will determine whether to sell ($P_G < 0$) or purchase ($P_G > 0$) energy from the AC utility grid. In the meantime, the BESS will compensate the power imbalance P_{OS} to maintain a stable V_{PCC}. Thus, the microgrid can be operated according to the discretized optimization formulae shown in (5) and (6) to minimize the electric bills.

$$\min\ C_{BESS_GC} = \sum_{P_G^n>0}^{N} \frac{P_G^n B}{\eta_G} + \sum_{P_G^n<0}^{N} \eta_G P_G^n B \quad (5)$$

subjected to

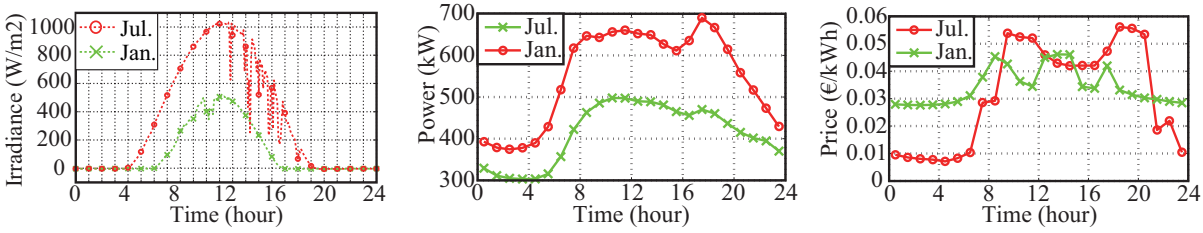
$$\begin{cases} P_{OS}^n = P_B^n & (6a) \\ \sum^N P_B^n \le \xi & (6b) \\ \left|P_B^n - P_B^{n-1}\right| \le \rho_B & (6c) \\ \left|P_G^n - P_G^{n-1}\right| \le \rho_G & (6d) \\ |P_G^n| \le P_{G_max} & (6e) \\ |P_B^n| \le P_{B_max} & (6f) \end{cases}$$

where B and η_G represent the real-time electricity prices and the conversion efficiency of the AC–DC converter, respectively. Here, $|\cdot|^n$ denotes the discrete value of variable $|\cdot|$ at the time step of n. Normally, N will cover the period of $T_D = 24$ h. Equation (6a) is the equality constraint of the generation-demand balance. In (6b), ξ is the tolerable deviation of the battery energy after a cycle of N. The state of charge (SOC) of the battery should be close to the initial SOC after a cycle of N. In inequality constraints of (6c) and (6d), the ramping rate of the battery power P_B and the DC source power P_G cannot exceed the the limits of ρ_B and ρ_G, respectively. In (6e) and (6f), P_{G_max} and P_{B_max} are the power limits of the DC source and battery, respectively.

In both the grid-connected and isolated operation, the battery capacity must be sufficient to ensure a stable operation of the grid for a given period of time. Therefore, the minimum battery capacity requirement can be calculated as

$$\begin{aligned} S^{BESS} = &\max \left[\sum_{P_{OS}^n<0}^{N} \frac{P_{OS}^n}{\eta_B} + \sum_{P_{OS}^n>0}^{N} \eta_B P_{OS}^n \right] \\ &- \min \left[\sum_{P_{OS}^n<0}^{N} \frac{P_{OS}^n}{\eta_B} + \sum_{P_{OS}^n>0}^{N} \eta_B P_{OS}^n \right],\ n \in (0, N) \end{aligned} \quad (7)$$

where η_B is the energy conversion efficiency of the BESS. According to (7), if the stored energy and delivered energy of the battery can be reduced, the required capacity of the battery can be reduced.



(a) Recorded solar irradiance patterns [23] (b) Scaled-down daily load profiles of a microgrid in Denmark [24]. (c) TOU electricity price in Denmark [24].

Fig. 2. Solar irradiance profiles, hourly-averaged load profiles and TOU electricity price profiles.

B. DC Microgrids with the Series ES

As shown in Fig. 1(b), the series ES and the NCL constitute a smart load unit to regulate V_{PCC} against the variation of P_{OS}. The series ES adjusts V_{NC} to manipulate the NCL current I_{NC} to reshape the profile of P_{NC} accordingly. When V_{PCC} is regulated at V_{ref}, P_{OS} is fully compensated by the smart load branch. Thus,

$$P_{OS} = V_{ref} \times (I_{NC} - I_{NC_nom}) \tag{8}$$

and

$$\begin{cases} P_{ES} = V_{ES} \times I_{NC} \\ I_{NC} = \dfrac{V_{ref} - V_{ES}}{R_{NC}} \end{cases} . \tag{9}$$

By combining (8) and (9), the corresponding P_{ES} is

$$P_{ES} = (P_{OS} + P_{NC_nom}) - \frac{(P_{OS} + P_{NC_nom})^2}{P_{NC_nom}} \tag{10}$$

Fig. 4(a) illustrates the power (P_{ES}) and voltage (V_{ES}) profiles of the series ES with respect to the ES current. Based on whether the series ES is boosting (when $P_{OS} < 0$, $V_{ES} > 0$) or suppressing (when $P_{OS} > 0$, $V_{ES} < 0$) V_{PCC}, and whether its battery is charged or discharged, the series ES can be operated correspondingly in boosting-discharging (BD), boosting-charging (BC), and suppressing-discharging (SD) mode. The absolute ratio of the ES power (P_{ES}) over the power change of smart load (ΔP_{SL}) can be defined as

$$\kappa = \left| \frac{P_{ES}}{\Delta P_{SL}} \right| \times 100\% = \left| \frac{V_{ref} - V_{ES}}{V_{ref}} \right| \times 100\% \tag{11}$$

The graph of κ versus V_{ES} in per-unit (P. U.) under the base of V_{ref} can be plotted as shown in Fig. 4(b).

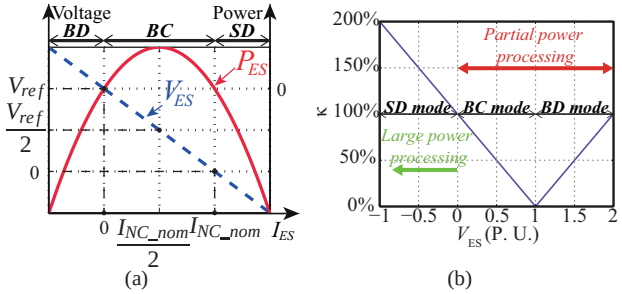
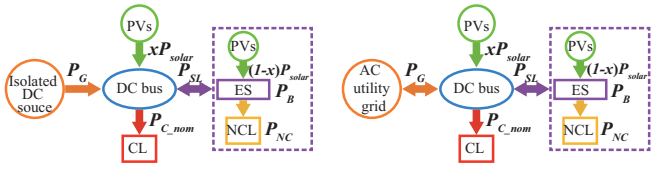


Fig. 4. (a) Operating curves of the series ES and (b) power exchange ratio of series ES with respect to V_{ES}.

When the series ES is boosting V_{PCC}, $\kappa < 100\%$. Therefore, the series ES will process partial power with the ability to shed the NCL. In this way, the required storage capacity to store the energy will be reduced. Nevertheless, when the series ES is suppressing V_{PCC}, $\kappa > 100\%$. The series ES delivers more power than the boosted power of the smart load. This will increase the battery capacity to deliver the energy. Therefore, a large storage capacity is needed for the voltage suppression operation.

C. DC Microgrids with the PV-Embedded Series ES

According to the analysis in Subsection III-B, it is the voltage suppression mode that increases the required storage capacity of the series ES. Nevertheless, the series ES is discharged during over-voltage condition ($P_{OS} > 0$), which is opposite to that of the BESS. This feature offers the possibility to the PVES in facilitating the buffering of excess solar energy through a smaller storage capacity. Fig. 1(c) shows the PVES system, in which $1-x$ of the total PV panels being shifted to the DC-link of ES. Fig. 5 illustrates the power flow paths of the PVES integrated DC grids.



(a) Isolated DC microgrids (b) Grid-connected DC microgrids

Fig. 5. Illustrations of power flow paths of PVES integrated DC microgrids.

The power balancing relationship can be formulated as

$$P_G + xP_{solar} = P_{C_nom} + P_{SL} \tag{12}$$

where P_{SL} is the power of the smart load and the variable x denotes the proportion of the grid-tied PVs' generation on the left of Fig. 1(c). The corresponding operating modes of BESS and PVES integrated microgrids are compared and analyzed as shown in Table I.

The battery power of the PVES can be derived using

$$\begin{aligned} P_B &= P_{ES} + (1-x)P_{solar} \\ &= (P_G + P_{solar} - P_{C_nom}) - \frac{(P_G + xP_{solar} - P_{C_nom})^2}{P_{NC_nom}} \end{aligned} \tag{13}$$

Therefore, the battery power P_B of the PVES system becomes an adjustable variable. Since some PVs are shifted from the PCC to the DC-link of the ES, the power generation

TABLE I
OPERATING MODES OF A INTEGRATED DC MICROGRID WITH BESS AND PVES

			BESS	PVES
	P_G	P_{OS}	P_{BESS}	P_{SL}
Isolated microgrids	constant	>0	>0	$>P_{NC_nom}$
	constant	<0	<0	$<P_{NC_nom}$
Grid-connected microgrids	<0	<0	<0	$<P_{NC_nom}$
	<0	>0	>0	$>P_{NC_nom}$
	>0	<0	<0	$<P_{NC_nom}$
	>0	>0	>0	$>P_{NC_nom}$

at the PCC is reduced. As a result, the ES will be operated frequently in the BC mode and process partial power to reduce the storage requirement. Meanwhile, the shifted PV panels can supplement the ES with energy in SD and BD mode to reduce the battery power output. Nevertheless, the ES battery must store energy from both the shifted PVs and the grid in the BC mode, which increases the storage capacity. Therefore, there will be an optimum shifting coefficient of $1-x$ which can lead to the minimum required storage capacity.

In an isolated DC microgrid, the minimum storage capacity can be achieved by minimizing the maximum stored or delivered energy of the battery. Therefore, the optimum shifting coefficient can be derived by solving the following discretized Minimax problem

$$\min_{x}\max_{t} S_{IS}^{PVES}=\left|\sum_{P_B^n<0}^{N}\frac{P_B^n}{\eta_B}+\sum_{P_B^n>0}^{N}\eta_B P_B^n\right| \tag{14}$$

subjected to (12), (13) and

$$\begin{cases} \sum^{N} P_B^n \le \xi & \text{(15a)}\\ \left|\sum^{N}[P_{SL}^n-(1-x)P_{solar}^n-P_{NC_nom}^n]\right|\le\varepsilon & \text{(15b)}\\ \left|P_{SL}^n-P_{SL}^{n-1}\right|\le\rho_{SL} & \text{(15c)}\\ |P_B^n|\le P_{B_max} & \text{(15d)}\\ 0\le x\le 1 & \text{(15e)}\\ 0\le n\le N & \text{(15f)} \end{cases}$$

Condition (15b) implies that the difference between the total NCL consumption with the PVES throughout N and the case without the PVES cannot exceed the limit of ε, i.e., the adoption of PVES cannot change the total power consumption of the NCL. Condition (15c) is the ramping rate constraint of the smart load.

Fig. 5(b) illustrates the power flow paths of a grid-connected DC microgrid with PVES. In grid-connected operation, for a specific $1-x$, the optimum battery power flow (P_B) and the corresponding required storage capacity can be derived from the equation

$$\min\ C_{PVES_GC}=\sum_{P_G^n>0}^{N}\frac{P_G^n B}{\eta_G}+\sum_{P_G^n<0}^{N}\eta_G P_G^n B \tag{16}$$

subjected to (12), (13), (15) and

$$\begin{cases} \left|P_G^n-P_G^{n-1}\right|\le\rho_G & \text{(17a)}\\ |P_G^n|\le P_{G_max} & \text{(17b)} \end{cases}$$

D. Numerical Calculation of Optimum $1-x$

Considering that (i) the load and irradiance data can be obtained from load estimation and weather forecasting and that (ii) the shifted amount of the PV modules are finite discrete values, the optimum $1-x$ and minimum required storage capacity S^{PVES} can be numerically and iteratively calculated. Fig. 6 shows the flowchart of a possible way of optimizing $1-x$.

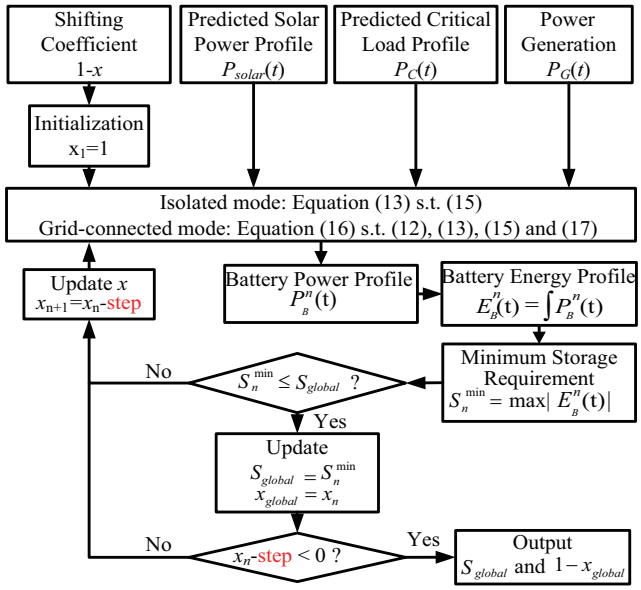


Fig. 6. Flow chart of deriving $1-x$

At the initialization step, the shifting coefficient is set as 0 (i.e., $x_1=1$). Based on the inputs of the generation and load profiles, the battery power profile $P_B(t)$ corresponding to the shifting coefficient $1-x_1$ can be derived using equation (13) (for isolated-mode) or (16) (for grid-connected mode). By integration, the required minimum storage capacity S_1^{min} corresponding to $1-x_1$ can be derived. The global optimum solutions will be temporarily set as $x_{global}=x_1$ and $S_{global}=S_1^{min}$. At the second step, the shifting coefficient will be updated to $1-x_2$ by adding one step, which equals the proportion of the single PV module among the PV system. Following the same procedure, S_2^{min} corresponding to $1-x_2$ can be derived. By comparing S_1^{min} and S_2^{min}, S_{global} will be updated to the smaller value between the two. In every iteration, $1-x_n$ will be increased by one step and S_{global} will be repetitively evaluated until all possible $1-x$ have been examined. In this way, the global minimum storage capacity S_{global} and the corresponding optimum $1-x$ can be derived.

IV. CIRCUIT ANALYSIS AND PRACTICAL CONSIDERATION OF PVES

A. Circuit Analysis of PVES

The shifted PV module connected to a DC-link battery is shown in Fig. 7. Considering that the voltage dynamics of the battery can be negligible [25], the DC-link voltage can be approximated to be a DC voltage V_B. i_{ESD} denotes the averaged current (over a switching cycle) flowing from the DC-link to

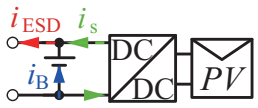


Fig. 7. Shifted PV module connected to a DC-link battery.

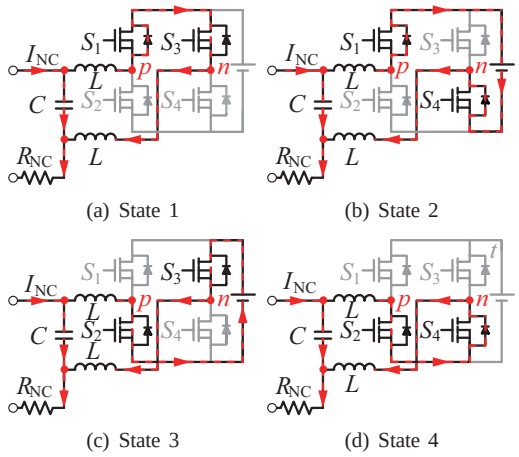
the grid side. With the MPPT control, the averaged injected current i_s of the shifted PV module can be calculated as

$$i_s = \frac{(1-x)P_{solar}}{V_B} \tag{18}$$

The battery current flowing from the cathode to the anode can be calculated by using

$$i_B = i_{ESD} - i_s \tag{19}$$

i_s is dependent on the solar irradiance and independent of the operation of ES converter (H-bridge). Two in-phase sawtooth carriers are adopted for the modulations of the two bridge branches and the switching states of the ES are analyzed in Fig. 8(a) to 8(d). The state 1 and 4 are the freewheeling states.



(a) State 1 (b) State 2

(c) State 3 (d) State 4

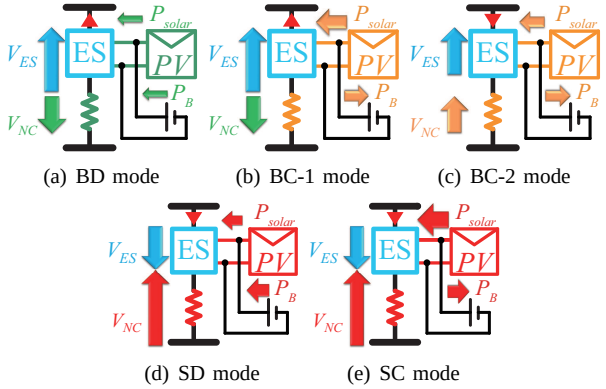
Fig. 8. Switching states of the ES converter. (Red arrows indicate the referenced current directions.)

TABLE II
OPERATING MODES OF PVES

Modes	Switching State	I_{NC}	V_{ES}	i_{ESD}	i_B
Idle	1 & 4	>0	$=0$	$=0$	$=0$
BD	1 & 2 & 4	<0	$>V_{PCC}$	>0	>0
BC-1	1 & 2 & 4	<0	$>V_{PCC}$	>0	<0
BC-2	1 & 2 & 4	>0	$<V_{PCC}$	<0	<0
SD	1 & 3 & 4	>0	<0	>0	>0
SC	1 & 3 & 4	>0	<0	>0	<0

The operating modes with respect to the switching states are analyzed in Table II. With the inclusion of PV modules to the DC-link, the PVES can be operated in six modes. In idle mode, $V_{ES} = 0$. The converter is switching in freewheeling states and the battery is electrically isolated from the grid. The other five operating modes are illustrated in Fig. 9.

There are three boosting modes, namely, BD, BC-1 and BC-2. The combinations of switching states are state 1, 2 and 4. In



(a) BD mode (b) BC-1 mode (c) BC-2 mode

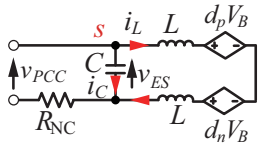
(d) SD mode (e) SC mode

Fig. 9. Illustration of circuit power flows in different operating modes.

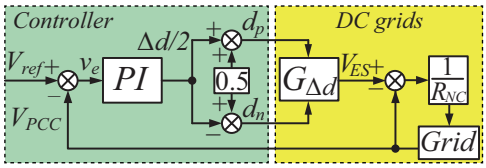
BD mode, $V_{ES} > V_{PCC}$ and $I_{NC} < 0$. Thus, battery is discharged in state 2 and the smart load injects power to the grid to boost V_{PCC}. In BC-1 mode, $V_{ES} > V_{PCC}$ and the DC-link is delivering energy to the grid in state 2. With the supplementary energy harnessed from the shifted PV modules, the battery is charged. In BC-2 mode, $0 < V_{ES} < V_{PCC}$. Both the shifted PV modules and grid are charging the battery. NCL is shed to boost V_{PCC}.

There are two suppression modes, namely, SD and SC mode. In the suppression modes, the switching state combinations are the freewheeling states and state 3. For all suppression modes, $V_{ES} < 0$ and the DC-link is delivering energy to the system in state 3. In SD mode, the shifted PV modules, grid and battery are boosting the NCL. In SC mode, the shifted PV modules deliver energy to both the NCL and the battery.

By averaging the ES converter over a switching cycle, the equivalent circuit can be plotted as shown in Fig. 10(a). The duty ratio of switch S_1 and S_3 are denoted as d_p and d_n.



(a) Averaged equivalent circuit of the smart load.



(b) Control block diagram of the smart load

Fig. 10. Averaged circuit model and control block diagram of the smart load.

Based on Fig. 10(a), the state-space averaged model of the smart load branch can be derived as

$$\begin{cases} \Delta d = d_p - d_n \\ \dfrac{di_L}{dt} = \dfrac{v_{ES} - \Delta d V_B}{2L} \\ C\dfrac{dv_{ES}}{dt} = i_C \\ \dfrac{v_{PCC} - v_{ES}}{R_{NC}} = i_C + i_L \end{cases} \tag{20}$$

Thus, Δd to v_{ES} small-signal transfer function can be derived as

$$G_{\Delta d} = \frac{v_{ES}}{\Delta d} = \frac{V_B R_{NC}}{2LCR_{NC}s^2 + 2Ls + R_{NC}} \quad (21)$$

$G_{\Delta d}$ is a typical second-order system. Fig. 10(b) shows a possible control scheme of the ES converter using the PI control.

B. Practical Considerations

In the implementation of the PVES, there can be four failure conditions, namely, (i) failure of the NCL, (ii) failure of the battery, (iii) failure of the shifted PV modules and (iv) failure of the ES converter. For case (i), when NCL is faulted, the filtering inductors of the ES converter will reduce the inrush fault current. Besides, the ES converter can act as a circuit breaker to trip the NCL from the grid by ceasing the switching actions. Therefore, a circuit breaker can be saved in this configuration. For case (ii), when the faulted battery is tripped from the DC-link, the ES converter can be operated in idle mode and the battery is electrically isolated from the smart load. In the maintenance of batteries, the NCL will not be affected. However, the ES will lose the voltage regulation capability at PCC. For case (iii), the PVES will be reduced to a series ES. For case (iv), the PVES will be dissembled into an isolated NCL and a PV module connected to a battery. The PV module will keep charging the battery. Therefore, the failure of ES converter will be critical and a reliable ES converter is required.

V. Experiment Results of Isolated DC Microgrids with BESS, Series ES and PVES

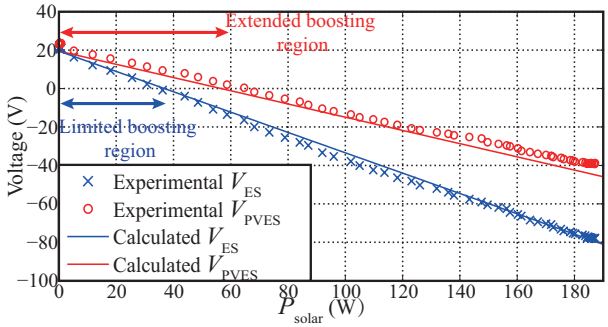
The circuit schematic diagrams of the BESS, series ES, and PVES integrated systems in the experimental work are shown in Fig. 11. A full-bridge converter is used for both the BESS and ES applications. The solar generation is emulated via a grid-interfaced full-bridge converter. The converter is controlled to inject a variable power, which is proportional to the solar irradiance, into the grid. The corresponding specifications are shown in Table III.

TABLE III
Parameters of the Variable Critical Load Integrated System

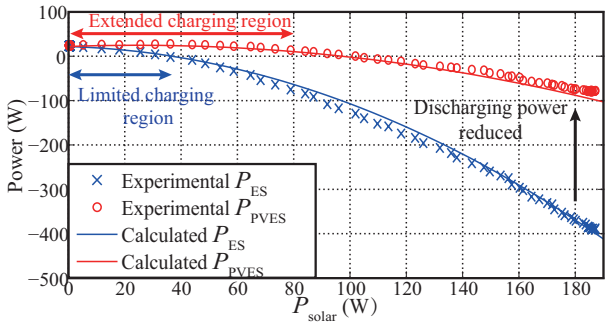
Description	Parameter	Value
Stable power source	V_G	50.3 V
Nominal PCC voltage	V_{ref}	48 V
Distribution cable resistance	R_L	0.8 Ω
IGBT switches	$S_{1,2,3,4}$	IRG4PC30FDPBF
Filter capacitor	C_{ES}	21 μF
Filter capacitor	C_{CL},C_{PV}	1 μF
DC-link capacitor	C_{DC}	150 μF
Filter inductor	L_f	3.3 mH
DSP controller		TMS320F28069
Maximum solar power	P_{solar_max}	189.33 W

A. Operating Curves of the PVES and the Series ES

In this experiment, both the NCL and CL are set to be 25.4 Ω. The peak solar generation is set at 189.33 W. The series ES and PVES are activated to buffer the solar power. From (12) to (15), around 31% of the total solar generation is shifted to the series ES. With the ES activated, V_{PCC} is regulated at 48 V. The corresponding measured voltage and power data of both types of ES are recorded and plotted against the variation of solar power in Fig. 12, along with the calculated curves obtained using equation (10) and (13). The measured experimental data fits the mathematically calculated curves with small deviations (around 10%), which are mainly introduced by sensing errors.



(a) Voltage curves of the series ES and PVES with respect to the change of P_{solar}



(b) Power curves of the series ES and PVES with respect to the change of P_{solar}

Fig. 12. Voltage and power curves of ES with respect to the change of P_{solar}.

As shown in Fig. 12(a), the operating voltage of the PVES is always greater than that of the series ES. The shifting of PV reduces the solar power being injected into the PCC and tends to cause more voltage sag. Thus, the voltage boosting region ($V_{ES} > 0$) increases as shown in Fig. 12(a) and the PVES is more likely to be operated in BC mode. This means that the ES has more possibility to use small storage capacity to boost the system voltage. Besides, in voltage suppression mode, the PVES generates a smaller compensating voltage than series ES. It means that the PVES discharges less power than series ES. In addition, since the voltage operation range of PVES is smaller than that of the series ES, the applied voltage of NCL will have a smaller variation.

By comparing the power curve of the series ES with that of the PVES shown in Fig. 12(b), it can be seen that the PVES enables a more even charging and discharging region than that of the series ES. This can lead to (i) a prolonged battery lifetime due to the reduced discharging rate and (ii) a balanced charging and discharging curve of the PVES against the variation of solar power generation.

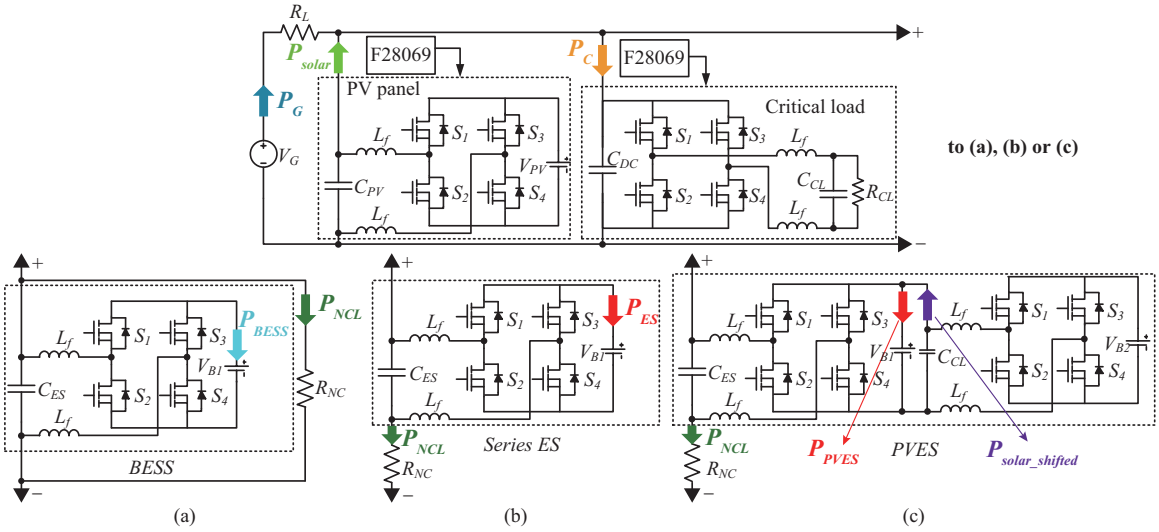
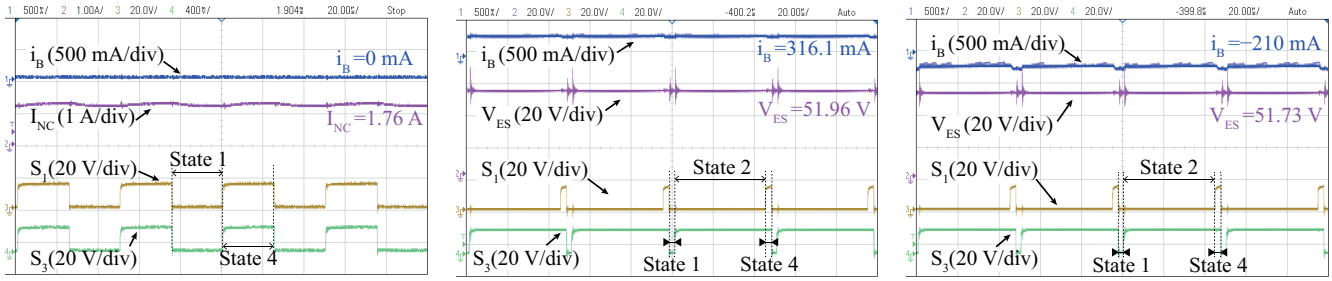


Fig. 11. Experiment setup of (a) BESS, (b) series ES and (c) PVES integrated DC grid.



(a) Idle mode ($V_G = 52.4$ V and battery is removed).

(b) BD mode ($V_G = 50$ V and $I_s = 0$ mA).

(c) BC-1 mode ($V_G = 50$ V and $I_s = 500$ mA).

(d) BC-2 mode ($V_G = 51.4$ V and $I_s = 500$ mA).

(e) SD mode ($V_G = 53.4$ V and $I_s = 500$ mA).

(f) SC mode ($V_G = 53.4$ V and $I_s = 1500$ mA).

Fig. 13. Experiment waveforms of the operating modes of the PVES.

B. Operating Modes of PVES

In this experiment, both the NCL and CL are set to be 25.4 Ω. The experimental waveforms of the six operating modes are shown in Fig. 13. The IGBT switches are turned on at low voltage and turned off at high voltage (15 V).

In the idle mode (Fig. 13(a)), the battery is removed from the DC-link. Since the PVES is switching between state 1 and 4, the NCL current is commutating between the upper switches (S_1 and S_3) and lower switches (S_2 and S_4) without flowing through the DC-link. Therefore, the DC-link current i_B is 0 A.

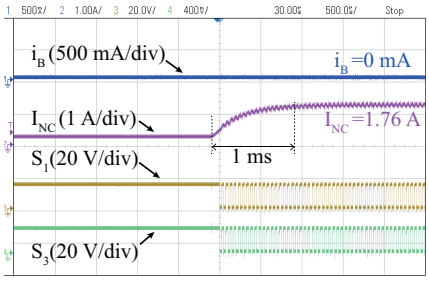
The waveforms of BD mode are shown in Fig. 13(b). When $V_G = 50$ V, the ES outputs a DC voltage of 51.96 V to boost V_{PCC} to 48 V. Since $V_{ES} > V_{PCC}$, the NCL voltage and current will become negative. Besides the freewheeling states, the BD mode has an extra state 2, which allows the battery to discharge. The battery is delivering a current of 316.1 mA to supply both the system and the NCL.

In BC-1 mode (Fig. 13(c)), the ES converter is switching among states 1, 2 and 4. As the NCL current is negative, the DC-link is discharging power in state 2. However, with the PV emulator injecting a DC current of 500 mA to the DC-link, the battery is charged at a DC current of 210 mA.

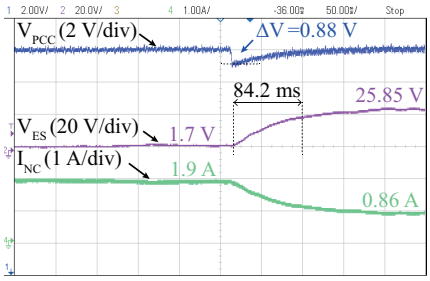
In BC-2 mode (Fig. 13(d)), the ES outputs a DC voltage of 26.6 V (< 48 V) to boost V_{PCC}. Since the NCL current is positive, the ES battery is charged in state 2. Thus, the PV emulator and the DC grid are charging the battery with a 650.7 mA DC current. For all boosting modes, the combinations of switching states are state 1, 2 and 4.

When $V_G = 53.4$ V, the PVES will output a DC voltage of -18 V to suppress V_{PCC}. In the suppressing mode, the NCL current is greater than the nominal value and the combinations of switching states are state 1, 3 and 4. In state 3, the current flows from the cathode to the anode of the DC-link to deliver power from the DC-link to the system. Therefore, when the injected current I_s is not large (500 mA) as shown in Fig. 13(e), the battery is discharged at 755 mA and the PVES is operated in SD mode. When I_s is large (1500 mA) as shown in Fig. 13(f), the battery is charged at 237.5 mA and the PVES is operated in SC mode.

C. Transient Responses of PVES



(a) Transient waveforms of the start-up of the PVES.



(b) Transient waveforms of PVES regulating V_{PCC}.

Fig. 14. Experiment waveforms of transient response of PVES.

The transient waveforms of the PVES in the start-up process are shown in Fig. 14(a). The PVES is operated from OFF state to idle state. Instead of stepping directly to the full load current, it takes around 1 ms for the I_{NC} to rise from 0 A to 1.76 A. In the meantime, the battery current is 0 A.

The transient waveforms of the PVES in voltage regulation operation are shown in Fig. 14(b). When V_{PCC} is stepped down by 0.88 V, it takes the PVES 84.2 ms to reach an output voltage of 25.85 V to restore V_{PCC} to 48 V. The I_{NC} is shed from 1.9 A to 0.86 A.

D. PV System with Variable Critical Load

In this experiment, the storage reduction ability of the PVES is verified through a scale-down DC grid. The CL is set to be a variable load as shown in Fig. 11. The NCL is constant resistive (37.5 Ω). The BESS and PVES are adopted to regulate the bus voltage respectively. The output of the DC source is set at 49.1 V and it delivers a constant power of 67 W to the grid when V_{PCC} is regulated to 48 V. As shown in Fig. 15(a), the solar generation generates the power in the time period from 49 s to 193 s and the CL is programmed to be fluctuating between 28.6 W and 96.7 W. We use a timescale of 10 seconds to represent 1 hour. The experiment is conducted for 240 s to simulate a day. The shifting coefficient is set at 34% and another full-bridge converter is used to emulate the shifted PV modules.

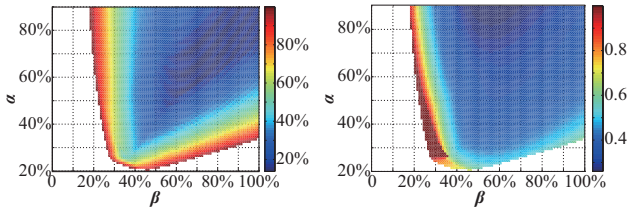
As shown in Fig. 15(b), without any load control, the BESS is operated to store energy in the period from 62 s to 163 s and to deliver energy from 160 s to 240 s. The maximum charging and discharging power can be found as 111.17 W and 96.28 W, respectively. Meanwhile, the power profile of the PVES is fluctuating between 50 W and -50 W. With 34% of the solar power being shifted to the ES, it can be observed that the discharging power of the PVES between 80 s and 160 s is not large (-18.8 W at most). This means the PVES system does not require the battery to be charged or discharged as fast as the BESS system in the same system configuration. This can extend the lifetime for the installed batteries [26].

The energy profiles of both the BESS and PVES are shown in Fig. 15(c), the maximum values of the energy profiles for the BESS and the PVES are respectively 7.16 kJ and 1.79 kJ. Thus, it can be concluded that the use of the PVES can effectively reduce the storage capacity required in a DC grid with a variable CL (around 74.9%'s reduction).

VI. System Simulations of DC Microgrids with BESS and PVES

A. Isolated DC Microgrids

The simulations are repeated with different sets of α and β to evaluate the variation of $1-x$ and the storage reduction capacity of PVES in isolated DC microgrids. We set the value of α within the section of 20% to 90% and β between 0% and 100%.

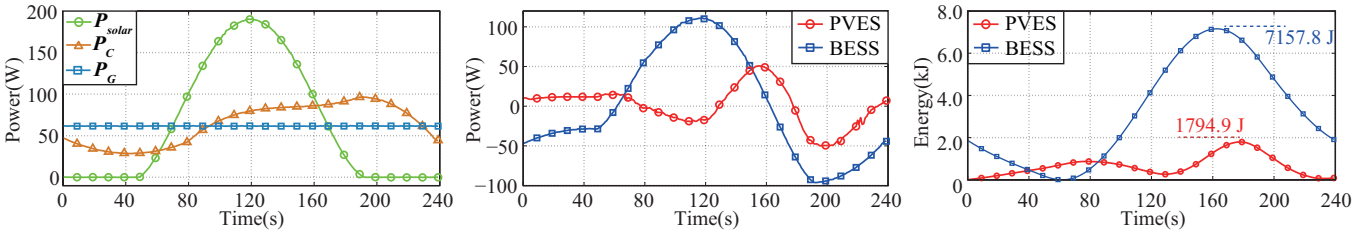


(a) Relative storage capacity of PVES against the storage capacity of BESS

(b) Shifting coefficient $1-x$

Fig. 16. Relative storage capacity of PVES and shifting coefficient $1-x$ with respect to the change of α and β.

Fig. 16(a) illustrates the plot of relative storage capacity of the PVES system with respect to the change of α and β. The color temperature is used to indicate the value of the relative storage capacity of the PVES against that of the BESS system. When $0 \leq \alpha \leq 20\%$ or $0 \leq \beta \leq 20\%$ (blank space shown in Fig. 16(a)), the storage capacity of the PVES system is greater than that of BESS system. Thus, it can be concluded that the PVES is ineffective in reducing the energy storage with a small α or a small β. As shown in Fig. 16(a), when both α and β increase, the relative storage capacity reduces. This means that



(a) Power profiles of stable power supply, PV panel and critical load

(b) Power profiles of BESS and PVES

(c) Energy profiles of BESS and PVES

Fig. 15. Experiment waveforms of the BESS and PVES with a variable critical load.

higher values of α and β will lead to a larger reduction of the storage capacity.

Fig. 16(b) illustrates the optimum shifting coefficient with respect to the change of α and β. Judging from the color temperature, it can be seen that $1-x$ is within the section of 0.3 to 0.4 for most cases. This means that $1-x$ is not sensitive to the change of α and β for most cases.

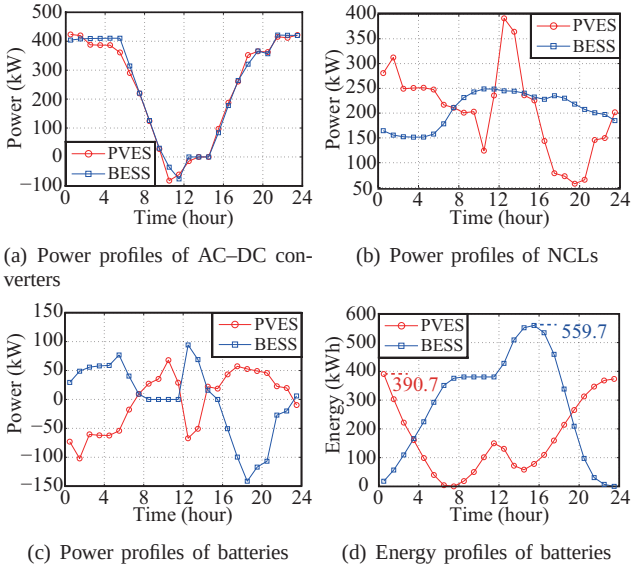
B. Grid-connected DC Microgrids

Simulations of a 400 kVA DC microgrid have been performed to compare the impacts of PVES and BESS on the (i) storage capacity, (ii) electric bills and (iii) power losses in grid-connected operations. The specifications of the corresponding parameters are listed in Table IV. The profiles of the solar irradiance, load and TOU electricity prices are shown in Fig. 2. Here, the data in July is used for the case study.

TABLE IV
SPECIFICATIONS OF THE VARIABLE CRITICAL LOAD INTEGRATED SYSTEM

Description	Parameter	BESS	PVES
Battery energy deviation tolerance	ξ	60 kWh	
NCL energy deviation tolerance	ε	1 kWh	
Smart load ramping rate limit	ρ_{SL}	NA	100 kW/h
Ramping rate of battery power	ρ_B	100 kW/h	
Ramping rate of source power	ρ_G	100 kW/h	
Power limit of the source	P_{G_max}	430 kW	
Power limit of the battery	P_{B_max}	430 kW	
Battery efficiency	η_B	90%	
AC–DC converter efficiency	η_G	90%	
NCL proportion	α	50%	
Solar penetration depth	β	50%	
shifting coefficient	$1-x$	4%	

As shown in Fig. 17(a), the profiles of P_G are similar for both BESS and PVES integrated DC grids. The microgrids purchase power in midnight when both the load and price are low, and sells power at noon when both the solar generation and price are high. Comparing the NCL profiles of the PVES integrated system with that of the BESS integrated system as shown in Fig. 17(b), the NCL is rescheduled from 08 : 00 to 22 : 00 (when both CL and price are high) to 00 : 00 to 07 : 00 (when both the CL is low) and 12 : 00 to 15 : 00 (when the solar generation is high). Besides, when both the CL and the price are high (16 : 00 to 21 : 00), the NCL with the PVES (red trace) is shed to around 50 kW. Consequently, the NCL profile is tamed to fill the valley and cut the peak, which reduces both the electric bills and storage capacity. The corresponding power and energy profiles of the batteries in BESS and PVES integrated system are respectively shown in Fig. 17(c) and Fig. 17(d). As shown in Fig. 17(d), the required minimum storage capacity for the BESS integrated system is 559.7 kWh, while the required storage capacity for the PVES integrated system is 390.7 kWh, which is 69.8% of the case of the BESS integrated system.



(a) Power profiles of AC–DC converters

(b) Power profiles of NCLs

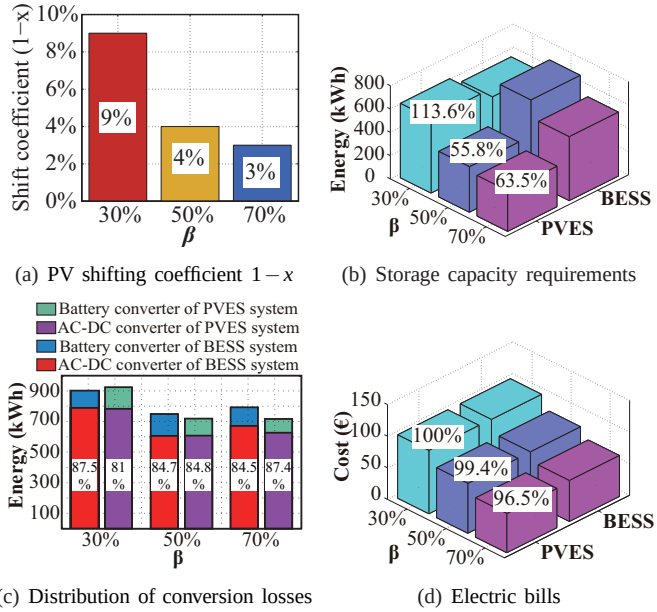
(c) Power profiles of batteries

(d) Energy profiles of batteries

Fig. 17. Simulation waveforms of DC grids when $\beta = 50\%$.

The capacity of the solar generation are set as 30%, 50% and 70% of the total generation respectively to represent a microgrid with small, medium and large solar generation. Fig. 18 illustrated the simulated results of shifting coefficient, required storage capacity, distribution of conversion losses and electric bills. The shifting coefficient is shown in Fig. 18(a). Compared with the cases of the isolated microgrids, the shifting coefficient of PVES integrated system is much smaller. In grid-connected operations, the excessive solar generation can be transferred to the utility grid. Thus, small amount of PVs are required to support the ES with the operation of voltage suppression. As shown in Fig. 18(b), the PVES can help reduce storage capacity in grids with medium ($\beta = 50\%$) and large ($\beta = 70\%$) solar generation. It requires 55.8% and 63.5% of the capacity of the BESS integrated system. However, when $\beta = 30\%$, the storage requirement of PVES is 113.6% of that of the BESS. Similar to the case of isolated DC

microgrids, the PVES cannot help reduce the required storage capacity when β is low.



(a) PV shifting coefficient $1-x$ (b) Storage capacity requirements

(c) Distribution of conversion losses (d) Electric bills

Fig. 18. Comparison of simulated results when β is set as 30%, 50% and 70% respectively.

The distribution of total conversion losses of the two types of grids are shown in 18(c). When $\beta = 30\%,\ 50\%$ and 70%, the power losses of the PVES integrated system are 102.5%, 96% and 90.4% of that of the BESS integrated system, respectively. Besides, according to Fig. 18(c), the power losses mainly come from the grid-interfaced AC–DC converter for both cases. Therefore, the PVES does not generate extra losses on the battery interfaced converter (ES converter) and it can even help in reducing the conversion losses. When P_{solar} is high, the PVES can transfer the excessive solar energy to the NCL instantly. However, for the BESS, P_{solar} is firstly stored in the battery and then released back to the loads. This increases the number of power processing stages and induces more conversion losses.

As shown in Fig. 18(d), the electric bills of the PVES integrated system are generally lower than that of the BESS integrated system. The reason is that the PVES can alter the power profile of the NCL in a real-time manner, which renders a less-stringent equality constraint of power balance. This improves the flexibility in the scheduling of P_G for the users to reduce the electric bills.

VII. Conclusions

In this paper, a new configuration of the PV-embedded series ES (PVES) is proposed to reduce the total energy storage capacity required in DC microgrids. A comparison of the storage requirements among the BESS, series ES and PVES integrated systems have been conducted. The storage optimization models for both isolated and grid-interconnected DC microgrid with BESS and PVES are formulated. The energy exchange status and circuit operating principles of the PVES are analyzed. Both the experiment and simulation results validate that the PVES can regulate the PCC voltage with less storage capacity against the variation of the solar generation and the critical load. The PVES is found to be a cost-effective measure for tackling the intermittency of solar power using a significantly smaller energy storage capacity in DC grids.

References

[1] G. F. Reed, "DC technologies: solutions to electric power system advancements [guest editorial]," *IEEE Power Energy Mag.*, vol. 10, pp. 10–17, Nov. 2012.

[2] J. Rajasekharan and V. Koivunen, "Optimal energy consumption model for smart grid households with energy storage," *IEEE J. on Sel. Topics Signal Process.*, vol. 8, pp. 1154–1166, Dec. 2014.

[3] A. Nagarajan and R. Ayyanar, "Design and strategy for the deployment of energy storage systems in a distribution feeder with penetration of renewable resources," *IEEE Trans. on Sustain. Energy*, no. 99, pp. 1–8, 2015.

[4] J. Matheys, J.-M. Timmermans, J. Van Mierlo, S. Meyer, and P. Van den Bossche, "Comparison of the environmental impact of five electric vehicle battery technologies using LCA," *Int. J. of Sustain. Manuf.*, vol. 1, no. 3, pp. 318–329, 2009.

[5] "IEEE recommended practice for sizing lead-acid batteries for stand-alone photovoltaic (PV) systems - redline," *IEEE Std 1013-2007 (Revision of IEEE Std 1013-2000) - Redline*, pp. 1–58, Jul. 2007.

[6] Y. Ru, J. Kleissl, and S. Martinez, "Storage size determination for grid-connected photovoltaic systems," *IEEE Trans. on Sustain. Energy*, vol. 4, pp. 68–81, Jan. 2013.

[7] S. Kawachi, J. Baba, T. Kikuchi, E. Shimoda, S. Numata, E. Masada, and T. Nitta, "Energy capacity reduction of energy storage system in microgrid stabilized by cascade control system," in *Euro. Conf.on Pow. Electron. and Applica.*, pp. 1–10, Sep. 2009.

[8] Z. Wang, C. Gu, F. Li, P. Bale, and H. Sun, "Active demand response using shared energy storage for household energy management," *IEEE Trans. on Smart Grid*, vol. 4, pp. 1888–1897, Dec. 2013.

[9] H. Mahmood, D. Michaelson, and J. Jiang, "Decentralized power management of a PV/battery hybrid unit in a droop-controlled islanded microgrid," *IEEE Trans. on Pow. Electron.*, vol. 30, pp. 7215–7229, Dec. 2015.

[10] M. Datta, T. Senjyu, A. Yona, T. Funabashi, and C.-H. Kim, "A coordinated control method for leveling PV output power fluctuations of PV–diesel hybrid systems connected to isolated power utility," *IEEE Trans. on Energy Convers.*, vol. 24, pp. 153–162, Mar. 2009.

[11] A. Luna, N. Diaz, L. Meng, M. Graells, J. Vasquez, and J. Guerrero, "Generation-side power scheduling in a grid-connected DC microgrid," in *IEEE Int. Conf. on DC Microgrids (ICDCM)*, pp. 327–332, Jun. 2015.

[12] Y. Yang, F. Blaabjerg, and H. Wang, "Constant power generation of photovoltaic systems considering the distributed grid capacity," in *Appl. Pow. Electron. Conf. and Expo. (APEC)*, pp. 379–385, Mar. 2014.

[13] A. Ahmed, R. Li, S. Moon, and J.-H. Park, "A fast PV power tracking control algorithm with reduced power mode," *IEEE Trans. on Energy Convers.*, vol. 28, pp. 565–575, Sep. 2013.

[14] S. Kawachi, J. Baba, H. Hagiwara, E. Shimoda, S. Numata, E. Masada, and T. Nitta, "Energy capacity reduction of energy storage system in microgrid by use of heat pump: characteristic study by use of actual machine," in *Int. Pow. Electro. and Motion Control Conf.*, pp. T11–52–T11–58, Sep. 2010.

[15] Y. Gu, X. Xiang, W. Li, and X. He, "Mode-adaptive decentralized control for renewable DC microgrid with enhanced reliability and flexibility," *IEEE Trans. on Pow. Electron.*, vol. 29, pp. 5072–5080, Sep. 2014.

[16] K. T. Mok, M. H. Wang, S. C. Tan, and S. Y. R. Hui, "DC electric springs – an emerging technology for DC grids," in *IEEE Appl. Pow. Electron. Conf. and Expo. (APEC)*, pp. 684–690, Mar. 2015.

[17] M. H. Wang, S. Yan, S. C. Tan, and S. Y. Hui, "Hybrid-DC electric springs for DC voltage regulation and harmonic cancellation in DC microgrids," *IEEE Trans. on Pow. Electron.*, vol. PP, no. 99, pp. 1–1, 2017.

[18] M. H. Wang, K. T. Mok, S. C. Tan, and S. Y. R. Hui, "Multifunctional DC electric springs for improving voltage quality of DC grids," *IEEE Trans. on Smart Grid*, vol. PP, no. 99, pp. 1–1, 2016.

[19] M. H. Wang, S. C. Tan, and S. Y. Hui, "Reduction of storage capacity in DC microgrids using pv-embedded series DC electric springs," in *IEEE Appl. Pow. Electron. Conf. and Expo. (APEC)*, pp. 3302–3309, Mar. 2016.

[20] E. M. S. D. of Hong Kong Special Administration Region, "Hong Kong energy end-use data 2015," pp. 43–44, Sep. 2015.
[21] L. Zhang, K. Sun, Y. Xing, L. Feng, and H. Ge, "A modular grid-connected photovoltaic generation system based on DC bus," *IEEE Trans. on Pow. Electron.*, vol. 26, pp. 523–531, Feb. 2011.
[22] K. Sun, L. Zhang, Y. Xing, and J. M. Guerrero, "A distributed control strategy based on DC bus signaling for modular photovoltaic generation systems with battery energy storage," *IEEE Trans. on Pow. Electron.*, vol. 26, pp. 3032–3045, Oct. 2011.
[23] NREL. [Online]: http://www.nrel.gov/midc/, Jan. 2016.
[24] Nord Pool. [Online]: http://www.nordpoolspot.com/Market-data1/Elspot/Area-Prices/, 2015.
[25] T. Yang, K. T. Mok, S. C. Tan, C. K. Lee, and S. Y. R. Hui, "Electric springs with coordinated battery management for reducing voltage and frequency fluctuations in microgrids," *IEEE Trans. on Smart Grid*, vol. PP, no. 99, pp. 1–1, 2016.
[26] D. Doerffel and S. A. Sharkh, "A critical review of using the peukert equation for determining the remaining capacity of lead-acid and lithium-ion batteries," *J. Power Sources*, vol. 155, no. 2, pp. 395–400, 2006.



Ming-Hao Wang (S'15) received the B.Eng. (Hons.) degree from Huazhong University of Science and Technology, Wuhan, China, and the University of Birmingham, Birmingham, U.K. in 2012. He received the M.Sc. degree from The University of Hong Kong, Hong Kong, in 2013. He is currently working toward the Ph.D. with the Power Electronics Research Group, Department of Electrical and Electronic Engineering, The University of Hong Kong, Hong Kong.

His research interests include smart grid technologies, AC-DC power conversion, DC power systems, electric springs and power electronics.



Siew-Chong Tan (M'06–SM'11) received the B.Eng. (Hons.) and M.Eng. degrees in electrical and computer engineering from the National University of Singapore, Singapore, in 2000 and 2002, respectively, and the Ph.D. degree in electronic and information engineering from the Hong Kong Polytechnic University, Hong Kong, in 2005.

From October 2005 to May 2012, he worked as Research Associate, Postdoctoral Fellow, Lecturer, and Assistant Professor in Department of Electronic and Information Engineering, Hong Kong Polytechnic University, Hong Kong. From January to October 2011, he was Senior Scientist in Agency for Science, Technology and Research (A*Star), Singapore. He is currently an Associate Professor in Department of Electrical and Electronic Engineering, The University of Hong Kong, Hong Kong. Dr. Tan was a Visiting Scholar at Grainger Center for Electric Machinery and Electromechanics, University of Illinois at Urbana-Champaign, Champaign, from September to October 2009, and an Invited Academic Visitor of Huazhong University of Science and Technology, Wuhan, China, in December 2011. His research interests are focused in the areas of power electronics and control, LED lightings, smart grids, and clean energy technologies.

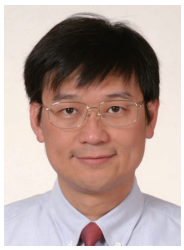
Dr. Tan serves extensively as a reviewer for various IEEE/IET transactions and journals on power, electronics, circuits, and control engineering. He is an Associate Editor of the IEEE Transactions on Power Electronics. He is a coauthor of the book *Sliding Mode Control of Switching Power Converters: Techniques and Implementation* (Boca Raton: CRC, 2011).



Chi-Kwan Lee (M08-SM14) received the B.Eng. and Ph.D. degrees in electronic engineering from the City University of Hong Kong, Hong Kong, in 1999 and 2004, respectively.

He was a Post-Doctoral Research Fellow with the Power and Energy Research Center, National University of Ireland, Galway, Ireland, from 2004 to 2005. In 2006, he joined the Center of Power Electronics, City University of Hong Kong, as a Research Fellow. He has been a Visiting Researcher with Imperial College London, London, U.K., since 2010. He was a Lecturer of Electrical Engineering with The Hong Kong Polytechnic University, Hong Kong, from 2008 to 2011. He is currently an Assistant Professor with Department of Electrical and Electronic Engineering, The University of Hong Kong, Hong Kong. His current research interests include wireless power transfer, clean energy technologies, and smart grids.

Dr. Lee received the IEEE Power Electronics Transactions First Prize Paper Award for his publications on Mid-Range Wireless Power Transfer in 2015. He is a Co-Inventor of the Electric Springs and planar EMI filter.



S. Y. (Ron) Hui (M87-SM94-F03) received his BSc (Eng) Hons at the University of Birmingham in 1984 and a D.I.C. and PhD in Electrical and Electronic Engineering at Imperial College London in 1987. Presently, he holds the Philip Wong Wilson Wong Chair Professorship at the University of Hong Kong and a part-time Chair Professorship at Imperial College London.

He has published over 300 technical papers, including more than 230 refereed journal publications. Over 60 of his patents have been adopted by industry. He is an Associate Editor of the IEEE Transactions on Power Electronics and IEEE Transactions on Industrial Electronics, and an Editor of the IEEE Journal of Emerging and Selected Topics in Power Electronics. His inventions on wireless charging platform technology underpin key dimensions of Qi, the world's first wireless power standard, with freedom of positioning and localized charging features for wireless charging of consumer electronics. He developed the Photo-Electro-Thermal Theory for LED Systems. He received the IEEE Rudolf Chope R&D Award from the IEEE Industrial Electronics Society and the IET Achievement Medal (The Crompton Medal) in 2010, and IEEE William E. Newell Power Electronics Award in 2015. He is a Fellow of the Australian Academy of Technological Sciences & Engineering and also a Fellow of the Royal Academy of Engineering, U.K.